

Dynamic surface phases controlling asymmetry of high-rate lithiation and delithiation in phase-separating electrodes

Bonho Koo^{1,7}, Jinkyu Chung^{1,7}, Juwon Kim^{1,7}, Dimitrios Fraggedakis², Sungjae Seo¹, Chihyun Nam¹, Danwon Lee¹, Jeongwoo Han¹, Sugeun Jo¹, Hongbo Zhao², Neel Nadkarni², Jian Wang³, Namdong Kim⁴, Markus Weigand⁵, Martin Z. Bazant^{2,6,8}, Jongwoo Lim^{1,8}

¹*Department of Chemistry, Seoul National University, Seoul 08826, South Korea*

²*Department of Chemical Engineering, Massachusetts Institute of Technology, Cambridge, MA 02139, USA*

³*Canadian Light Source Inc., Saskatoon, Saskatchewan S7N 0X4, Canada*

⁴*Pohang Accelerator Laboratory, Jigokro-127-beongil, Pohang, Gyeongbuk 790-834, South Korea*

⁵*Helmholtz-Zentrum Berlin (HZB), Albert-Einstein-Straße 15, Berlin 12489, Germany*

⁶*Department of Mathematics, Massachusetts Institute of Technology, Cambridge, MA 02139, USA*

⁷*These authors contributed equally to this work.*

⁸*Corresponding author. E-mail: jwlim@snu.ac.kr, bazant@mit.edu*

Supplementary section 1. *Operando* scanning transmission x-ray microscopy (STXM) platforms

1-1. Electrochemistry chip fabrication

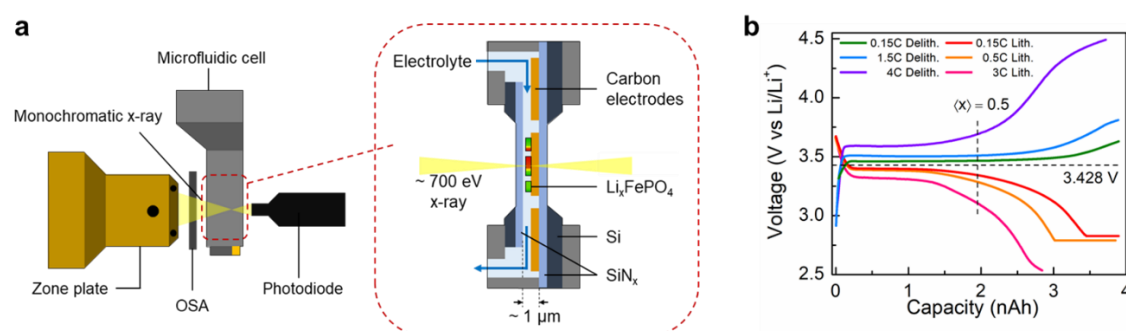
Electrochemistry chips in the microfluidic cell were microfabricated through the following procedure. First, a silicon wafer (4-inch diameter and 200 μm thickness) was cleaned with $\text{NH}_4\text{OH}/\text{H}_2\text{O}_2$ at 50°C (10 min), $\text{HCl}/\text{H}_2\text{O}_2$ at 70°C (10 min) and diluted HF (50:1, 1 min). After cleaning, low stress SiN_x (150 nm thickness) was deposited on the wafer through low pressure chemical vapor deposition method. Then, standard photolithography was conducted on the backside of Si/ SiN_x wafer to define X-ray transparent SiN_x membrane window.

The defined SiN_x window pattern on the backside was etched using inductively coupled plasma etcher to expose the Si for KOH wet etching. After removing the patterned photoresist (PR) in acetone, Si-exposed wafers were dipped into 1:3 weight ratio (KOH:DI water) KOH aqueous solution at 80°C to etch Si and create SiN_x membrane window (450 \times 20 μm). The chip dimension is 4.85 \times 6.35 mm. Photolithography was conducted on the topside of the window-defined wafer to pattern current collector (CC) pad on the electrochemistry chip.¹ The photolithography process was followed by spin coating, soft bake, UV exposure, post exposure bake using a negative tone PR (SU-8 2000.5).

1-2. Particle loading on the Electrochemistry chip

As-synthesized single crystalline LFP particles were dispersed in isopropyl alcohol (IPA), and ultrasonication was served to avoid aggregation. Then, dispersed particles in IPA were drop-casted and spin-coated on the working electrode on the Electrochemistry chip. Aggregated particles on the chip were stamped out by polydimethylsiloxane (PDMS) to make a single layer of LFP particles on the electrode. The number of LFP particles on the working electrode in the chip was approximately estimated through optical microscope ($10^4\sim 10^5$). The LiFePO_4 particles were coated with carbon through chemical vapor deposition method while the PR was carbonized simultaneously, forming carbon current collector.

1-3. *Operando* STXM experiment in microfluidic cell

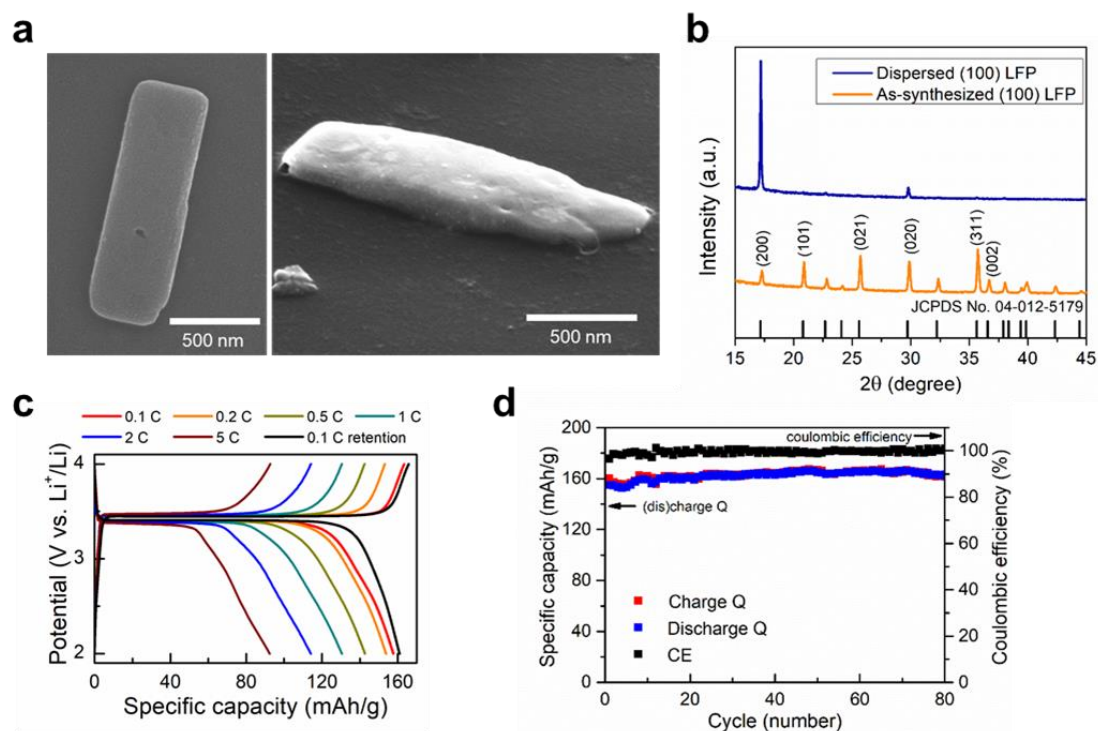


Supplementary Fig. 1 Schematics of *operando* STXM experiment. **a**, (Left) Schematics of beam path of synchrotron x-ray, the microfluidic cell, and STXM optics for *operando* imaging. (Right) Schematic cross-sectional view of the microfluidic cell. $\text{Li}_x\text{FePO}_4/\text{C}$ electrode on a microfabricated chip is placed in sandwiched SiN_x membrane where thickness between the membranes is $\sim 1 \mu\text{m}$. **b**, Multiple galvanostatic charge/discharge curves of [100]-oriented LFP/C electrode in the microfluidic cell during *operando* STXM experiment.

The microfluidic electrochemical cell consists of two microfabricated SiN_x membranes of the Electrochemistry and the spacer chip where liquid electrolyte flows through the gap of $\sim 1 \mu\text{m}$ as shown in Supplementary Fig. 1(b). For *operando* STXM experiments, we used 1 M LiClO_4 in ethylene carbonate/dimethyl carbonate (EC/DMC, 1:1 volume ratio).

To estimate faradaic capacity of the active materials, [100]-oriented LFP, on the microfabricated electrode, which contains the number of particles $10^4 \sim 10^5$, galvanostatic current $\sim 1 \text{ nA}$ was applied to the working electrode. Once the capacity was confirmed by the first electrochemical cycling, the working electrode was charged and discharged with various C-rates during *operando* STXM experiments. Galvanostatic (de)lithiations of the LFP Electrochemistry chip showed a typical electrochemical voltage plateau, small portion of non-faradaic capacity less than 5% at various C-rate, and reasonable rate-capabilities as shown in Supplementary Fig. 1(c). We concluded that *operando* electrochemistry STXM platform is well-functional and representable for coin cells.

Supplementary section 2. Characterizations of [100]-oriented LFP microplatelet single particle.



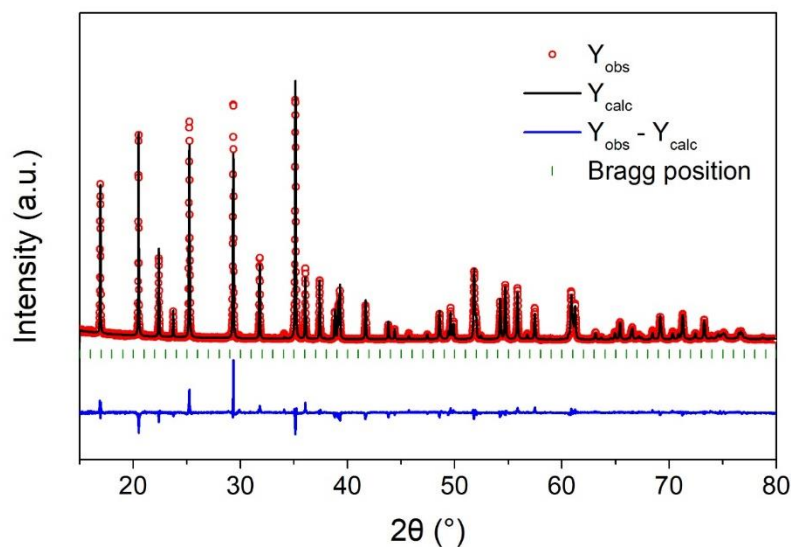
Supplementary Fig. 2 Validation of [100]-oriented LFP single particle. **a**, (Left) SEM image of as-synthesized [100]-oriented LFP particle. (Right) SEM image of the LFP particle at a 45-degree tilt. **b**, X-ray diffraction pattern of as-synthesized [100]-oriented LFP, and the LFP dispersed on silicon wafer substrate. **c**, **d** Electrochemical rate-capability (**c**) and cyclability (**d**) tests of the [100]-oriented LFP.

Synthesized [100]-oriented LFP microplatelet is about ~ 400 nm wide, ~ 1 μm long, and ~ 150 nm thick as shown in SEM images in Supplementary Fig. 2(a). Powder X-ray diffraction (XRD) patterns (orange-solid line) of the as-synthesized LFP well capture the theoretical XRD features of LFP (black-vertical lines, JCPDS No. 04-012-5179) in Supplementary Fig. 2(b).² Le bail fit results for power XRD data of [100]-oriented LFP are provided in Supplementary Section 3. For XRD patterns of the LFP dispersed on flat silicon wafer substrate (blue-solid line), the (200) intensity strongly manifests, which reflects the synthesized LFP has highly (100) preferred orientation.

In addition, we performed rate capability, capacity retention and cyclability tests for the synthesized LFP with LFP/Li half-cells, shown in Supplementary Fig. 2(c) and

(d). Specific capacity of the synthesized LFP was ~ 160 mAh/g, the capacity was completely recovered at 0.1C after multiple rate-capability tests, and the initial capacity was maintained over ~ 80 cycles at 0.1C. This strongly supports that the synthesized [100]-oriented LFP particle is a suitable model material for investigating Li (de)insertion spatiodynamics with negligible defects.

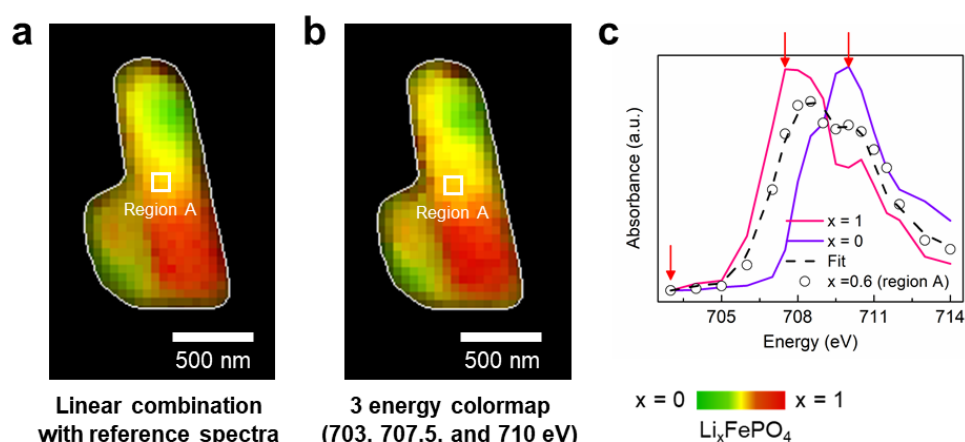
Supplementary section 3. Refinements of power X-ray diffraction (XRD)



Supplementary Fig. 3 Le bail fit results of the synchrotron XRD patterns of as-synthesis [100]-orientated LFP primary particles. Le bail fit was conducted with structure corresponds to Pnma space group (No.62).

XRD data was measured at beamline 9B at Pohang Light Source, South Korea. A wavelength of incident X-ray was 1.5226 Å, 2θ range was 10° – 131° , and the step size was 0.01° . Le Bail fit was performed using the TOPAS software.³ Lattice parameters are $a = 10.3262(3)$, $b = 6.0052(3)$, $c = 4.6932(0)$, and Cell Volume = 291.0316(3) (Å³) with R_p : 7.88 R_{wp} : 10.27, R_{exp} : 5.87, GOF = 1.75. The unit cell volume 291.03 Å³ indicates negligible anti-site defects.⁴

Supplementary section 4. Quantification of oxidation states and Li concentration through STXM at L₃ absorption edge



Supplementary Fig. 4 Comparison of Li composition maps between linear combination of full spectra and 3 energy method. **a, b,** Li composition maps using fine energy points (full spectra) fitting (**a**) and three energy points fitting (**b**) are presented. **c,** X-ray absorption spectra in fully lithiated LFP (pink-solid line), fully delithiated LFP (violet-solid line), and Region A in Supplementary Fig. 4(a) and (b) (white circle). The absorption spectrum of Region A is fitted by the linear combination of two end-phase absorption spectra (pink/violet).

STXM at L₃ absorption edge offers superior chemical sensitivity for measuring nanoscale particles and local current density. This technique is particularly advantageous for analysing primary single particles, as 200 nm thick LiFePO₄ absorbs around 60% of the incident X-rays at the Fe L-edge, while only absorbing about 1% at the Fe K-edge used by hard X-ray TXM.⁵ Therefore, the Fe L-edge is highly sensitive to oxidation states, allowing to measure fewer energy points for accurate quantification compared to the K-edge of transition metals. In this regard, *operando* STXM has been employed as a cutting-edge technique not just for various energy storage materials,^{6–8} but also for many catalyst materials,^{9–11} significantly advancing our comprehension of nanoscale kinetics in chemical and electrochemical systems.

In this work, Li composition of [100]-oriented LFP single particles is quantified with ~40 nm spatial and ~30 s temporal resolution through STXM image analysis at Fe L₃ absorption edge. The exposure time for each pixel is typically ranges from 1 to 3

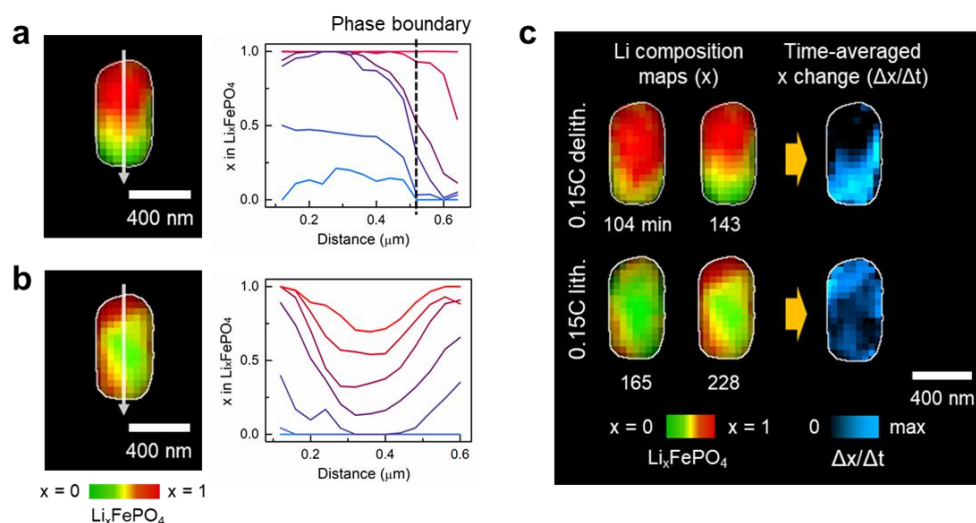
milliseconds, allowing for a full image scan of particles as large as 1-2 micrometres within 30 to 60 seconds. The pixelwise optical density (OD) is linearly fitted by the reference absorption spectra at Fe L₃-edge of fully-lithiated (Fe²⁺) and fully-delithiated (Fe³⁺) LFP. Here, two different quantification methods were carried out; the pixelwise OD was fitted by linear combination of two reference absorption spectra with 1) fine energy points (17 points), or 2) three energy points of 703, 707.5, and 710 eV. To validate two linear combination methods, region A was specified, white boxes in Supplementary Fig. 4(a) and (b). L₃-edge absorption of region A is plotted as circular symbols in Supplementary Fig. 4(c), and the linearly combined spectrum (a black-dashed line) accurately fits the absorption data. Fine energy points and three energy points methods showed the sufficiently similar Li distributions as shown in Supplementary Fig. 4(a) and (b). Thus, to increase temporal resolution during *operando* STXM, the linear combination with three energy points were used for the quantification.

Pixelwise X-ray absorptions at 707.5 and 710 eV are calculated by subtraction of the optical density at the pre-edge energy point 703 eV from those at 707.5 and 710 eV, respectively. The relative amount of Li-rich and Li-poor composition, x and y , is determined by the following equation,

$$\begin{bmatrix} I_{707.5} \\ I_{710} \end{bmatrix} = \begin{bmatrix} \epsilon_{707.5}^{LFP} & \epsilon_{707.5}^{FP} \\ \epsilon_{710}^{LFP} & \epsilon_{710}^{FP} \end{bmatrix} \begin{bmatrix} a \\ b \end{bmatrix}. \quad (1)$$

Here, I_E represents the pixelwise absorption at the energy of E , and ϵ_E^{LFP} and ϵ_E^{FP} indicate the absorption coefficients of the end-member spectra (LFP and FP) at the energy of E . Li concentration x in Li _{x} FePO₄ is then calculated from $x = \frac{a}{a+b}$. The hue and brightness in Li composition maps in Fig.3-5 in the main text represent x and $a + b$, respectively.

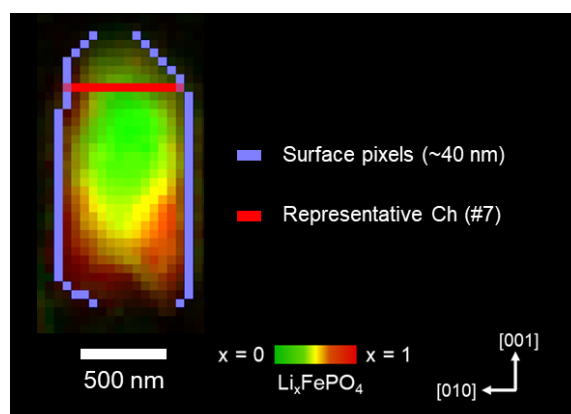
Supplementary section 5. Li composition change during 0.15C (de)lithiation



Supplementary Fig. 5 Line cuts of Li composition and time-averaged composition change in Li_xFePO_4 single particles during 0.15C (de)lithiation. **a** and **b**, Representative particle and corresponding line cuts profile along the white arrow are plotted during 0.15C delithiation (**a**) and lithiation (**b**) respectively (**c**) Time-averaged Li composition change between two consecutive Li maps during 0.15C (de)lithiation. Blue colour indicates a relative scale of the composition change rates.

At 0.15C delithiation, line cuts of Li composition in Supplementary Fig. 5(a) shows the full extraction of Li channels at the bottom of the particle and clear phase boundaries between Li-rich and poor phase, representing channel-by-channel kinetics. In contrast, during 0.15C lithiation in Supplementary Fig. 5(b), Li fills up from the surface region, but the whole channels are not fully lithiated, showing more uniform Li distribution. The composition gradients in the [010] channels are much smoother during lithiation than that during delithiation. Line cuts clearly reflect that lithiation occurs homogeneously along the [010] channels while delithiation drives strong phase separation and *domino-cascade* features.

Supplementary section 6. Definition of 1) pixelated channels (Chs) and 2) the surface/internal pixel of STXM image

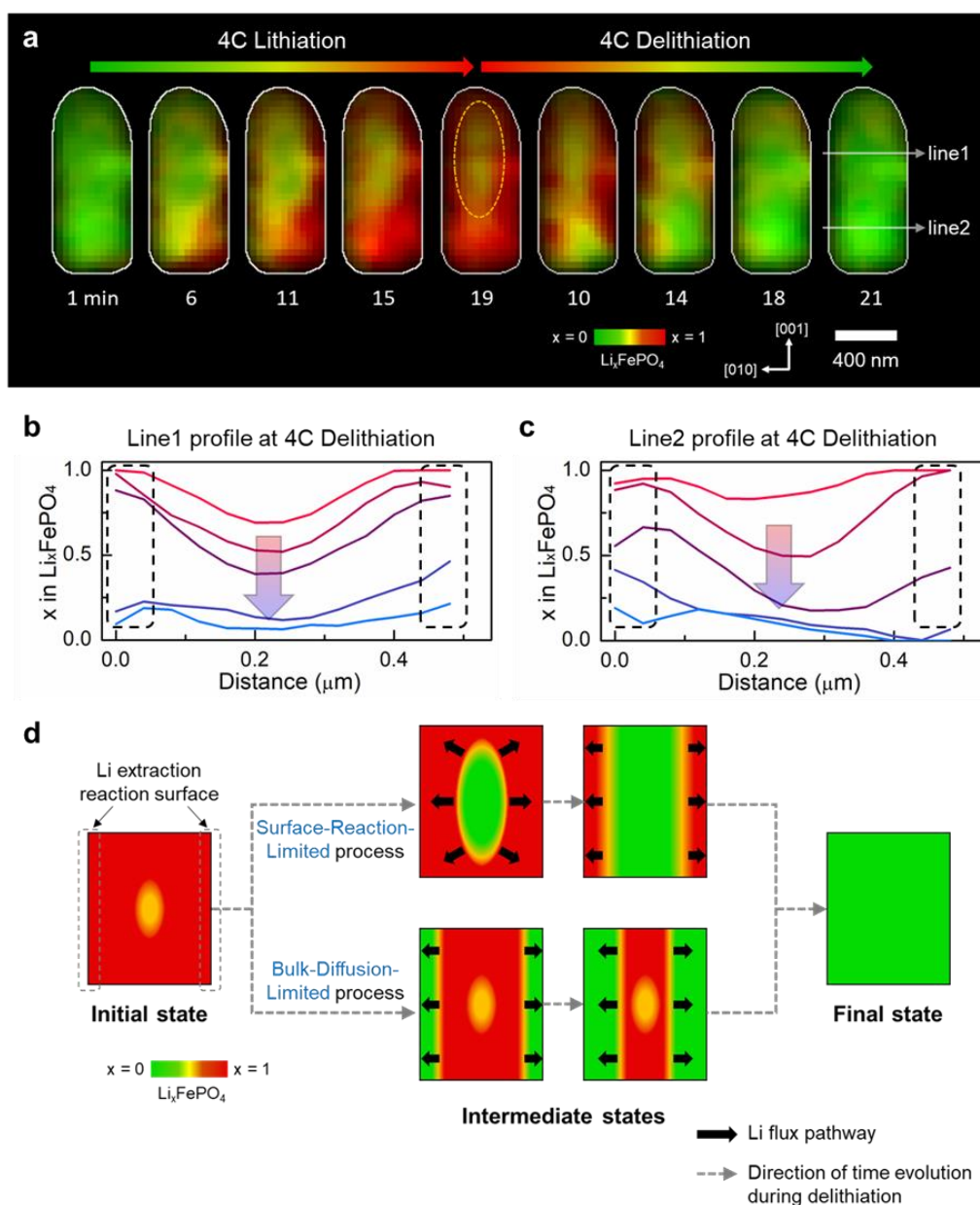


Supplementary Fig. 6 A representative pixelated channel (Ch) and the surface pixels of [100]-oriented LFP primary particle. A representative Ch (red) and the surface pixel (violet) are specified in the LFP particle. The internal pixels are the complement of the surface pixels within the single particle.

We termed an array of pixels along the [010] direction at ~40 nm resolution as a *pixelated channel* (Ch) (red-coloured pixels in Supplementary Fig. 6). To specify Chs, Li map frames were rotated with respect to the particle morphologies. The long edge side of the particle was maintained parallel to the vertical axis, and the short side edge was assumed to be parallel to the [001] direction based on the statistical TEM analysis.

In addition, the surface pixel was defined as a group of edge pixels at the [010] facet within the single particles (marked in violet in Supplementary Fig. 6). The internal pixel was defined as the remaining part, except for the surface pixels within the entire particle pixel. Here, the pixel-wise particle boundary was confined under the following criterion of brightness: $a + b > 0.15$ (see Supplementary Section 4). The surface pixels of the Chs were also defined as two edge pixels of the Chs, where the violet and red pixels overlap in Supplementary Fig. 6.

Supplementary section 7. *Operando* STXM experiment at 4C (de)lithiation for specifying the rate determining step



Supplementary Fig. 7 *Operando* STXM results to identify the rate determining step.

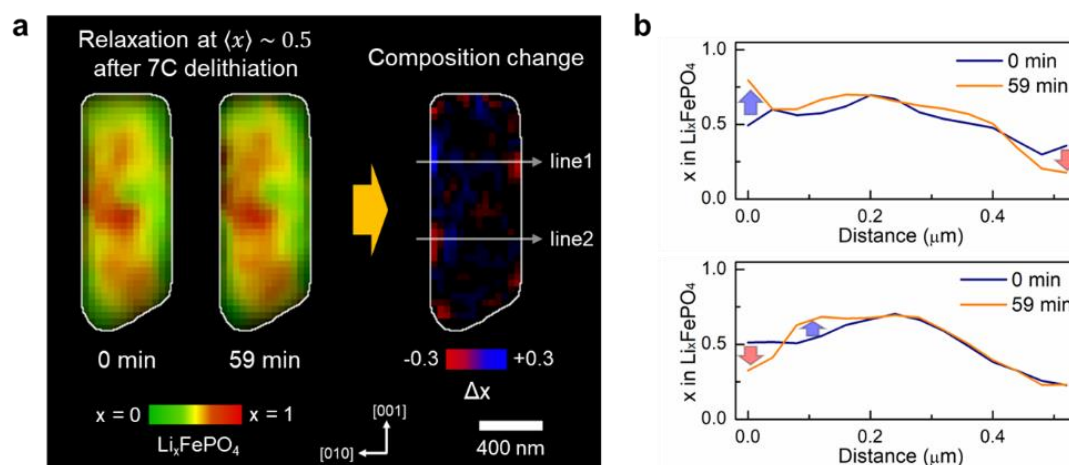
a, Representative Li maps of a [100]-oriented LFP during electrochemical (de)lithiation at 4C. We intentionally left the pre-delithiated core region (orange-dashed oval in **(a)**) after 4C lithiation to precisely locate the formation of Li-poor phase during 4C delithiation. **b**, **c** Corresponding line cuts of Li composition during 4C delithiation along line 1 **(b)** and line 2 **(c)**, shown in **(a)**. **d**, Schematics of phase transformation pathway of a particle with the pre-delithiated core under SRL and BDL process.

For phase-separating materials, surface-reaction-limited (SRL) and bulk-diffusion-limited (BDL) process drive a sharp diffusional front of the Li composition near the surface region.^{12,13} Thus, concurrent Li-rich and Li-poor domains near the surface regions, as shown in Fig. 5(a), complicate the identification of the rate-determining step (RDS) during high-rate (de)insertion reactions. To specify the RDS at high C-rates, we designed *operando* STXM experiments of [100]-oriented LFP particles at 4C delithiation, where the LFP particle had a pre-delithiated core region after fast 4C lithiation (Supplementary Fig. 7(a)). With a pre-delithiated core, triggering inhomogeneity in the interfacial energy within the particle and effectively lowering the nucleation barrier of the early transition of Li-poor domains is possible.

As depicted in the schematics of Supplementary Fig. 7(d), with delithiation being limited by the surface reaction, Li in the core region is extracted because the nucleation barrier of the Li-poor phase at the pre-delithiated core is lower than that at the Li-rich surface region, and the expansion of a single domain at the core has a much lower interfacial energy. In contrast, if delithiation was limited by bulk transport, the composition at the surface region would rapidly become Li-deficient and gradually become zero while the entire reaction surface was activated. The existence of the pre-delithiated core enabled precise localisation of the delithiation domains and determined the RDS between the SRL and BDL.

Our observations from Supplementary Fig. 7(a) indicate that the pre-delithiated core expands to the surface region, while the region becomes more delithiated. Line cuts of Li composition in Supplementary Fig. 7(b) and (c) support that Li ions are mainly extracted at the core region, and Li composition at the surface region remains populated by Li during overall 4C delithiation. This result indicates that bulk transport in the [010] channels in LFP is fast enough to keep up with the 4C reaction, and the characteristic reaction timescale at 4C is much greater than the diffusion timescale in LFP. Thus, we conclude that our *operando* STXM results are within the regime of the SRL process.

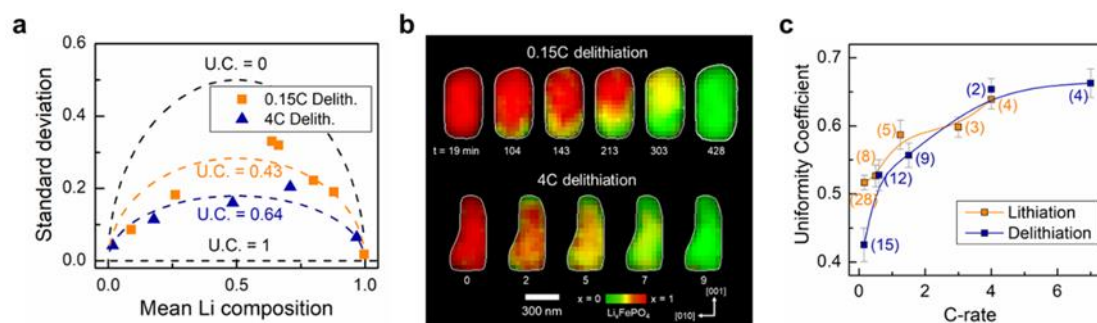
Supplementary section 8. Li composition change during ~1 h relaxation right after 7C delithiation



Supplementary Fig. 8: Representative Li map from *operando* STXM during ~1 h relaxation at $\langle x \rangle \approx 0.5$ of Li_xFePO_4 after 7C delithiation. **a**, Li composition maps of LFP primary particles during relaxation at $\langle x \rangle \approx 0.5$ of Li_xFePO_4 after 7C delithiation. Li maps of composition change during the relaxation are shown at the right (red: -0.3 and blue: +0.3). Li diffusion more occurs from Li-poor to Li-rich regions towards phase-separation during relaxation. **b**, Corresponding line cuts of Li composition along line 1 and 2 in (a).

We performed *operando* STXM at 7C delithiation and relaxation immediately after the delithiation. Supplementary Fig. 8(a) shows the Li composition maps and their changes during ~1 h of relaxation, where the increase and decrease in Li concentration during the relaxation are marked with blue and red, respectively. Notably, the Li composition changes preferentially in the surface region. The Li concentration at the delithiated surface region is reduced more during relaxation, indicating a further development of the Li-poor phase. In contrast, the Li composition in the lithiated surface region at $t = 0$ increases more during relaxation. Line cuts of the Li composition along line 1 and line 2 in Fig. 8(a) are plotted in Supplementary Fig. 8(b), supporting the nucleation of the stable phases near the surface region during relaxation.

Supplementary section 9. Uniformity coefficient calculation



Supplementary Fig. 9 Uniformity coefficient (UC) calculation of [100]-oriented LFP.

a, Standard deviations of pixelwise Li compositions within the particle Li maps as a function of mean Li composition of the particle. UC = 0 and 1 imply fully phase-separated and uniform solid-solution phases, respectively. **b**, Li composition maps during 0.15C and 4C delithiation process corresponding to **(a)**. **c**, UC of the particles during *operando* STXM as a function of C-rate. The value in parentheses indicates the number of particles in the same electrochemical process.

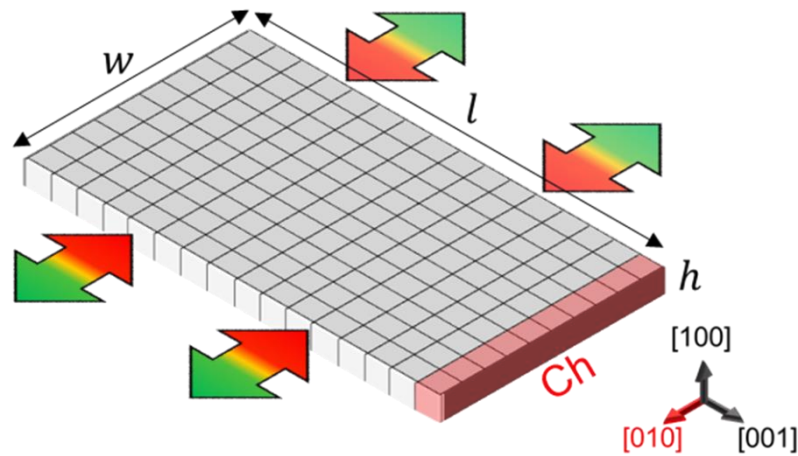
We define uniformity coefficient (UC) to describe how uniformly Li composition distributes within the particles during the overall (de)lithiation reaction.⁷ First, pixelwise standard deviation (SD) of Li composition is calculated, plotted as a function of $\langle x \rangle$ of the particles in Supplementary Fig. 9(a). Then, SD is fitted by the following equation (2) where $\sqrt{x(1-x)}$ represents the standard deviation curve of fully phase-separated particle at Li composition x .

$$SD(x) = A\sqrt{x(1-x)}. \quad (2)$$

Fitting parameter A is proportional to compositional heterogeneity. Therefore, UC is defined as 1-A where UC = 1 refers completely uniform Li distribution, and UC = 0 refers complete phase separation. In Supplementary Fig. 9(b), Li maps at the top and bottom row are representative Li maps at 0.15C and 4C delithiation, respectively. Their UCs are ~0.43 for 0.15C and ~0.64 for 4C, respectively, indicating Li extraction occurs more uniformly at higher C-rates. Supplementary Fig. 9(c) shows UC of the single particles tracked in *operando* STXM as a function of C-rate. At lower rates, Li distribution during delithiation shows more heterogeneity, or more phase-separation, than that during lithiation. At higher rates, solid-solution phase more appears within the particles, and UC

during both lithiation and delithiation becomes similar, which agrees with previous reports.¹⁴⁻¹⁶

Supplementary section 10. Calculation of exchange current density j_0 of Chs



Supplementary Fig. 10 Schematics of [100]-oriented LFP particle and the Chs

The exchange current density of Chs $j_{0\text{Ch}}$ within the single particle is calculated to determine precise (de)insertion reaction rates as a function of the surface Li composition x_{surf} . The exchange current density is calculated by the following procedures:

- 1) The pixelwise Li composition difference Δx is calculated between two sequential Li maps which were measured with the time interval Δt .
- 2) Δx is converted into ionic current density of the Ch j_{Ch} through the following equation (4),

$$j_{\text{Ch}} = e\rho_s \frac{V_{\text{pixel}}}{2hd} \frac{\sum \Delta x}{\Delta t} = \frac{1}{2} e\rho_s d \frac{\sum \Delta x}{\Delta t} \quad (4)$$

where e is the electron charge in Coulomb, ρ_s is the maximum volume concentration of Li sites in LFP ($1.38 \times 10^{28} \text{ m}^{-3}$), Δt is the time interval of the two sequential Li maps, h is thickness of the single particle, d is the width of a pixel, V_{pixel} is the volume of a pixel, and all pixelwise Δx are summed up within the Ch. Here, we hypothesized that Li composition change in Ch Δx_{Ch} is resulted solely from the current applied to the two edge-sides of the Ch during the reaction time-scale of our study.

- 3) By linearisation of BV equation under the overpotential limit of ~ 100 mV, the exchange current density $j_{0\text{Ch}}$ can be approximated by

$$j_{0\text{Ch}} = j_{\text{Ch}} \frac{RT}{F\eta}, \quad (4)$$

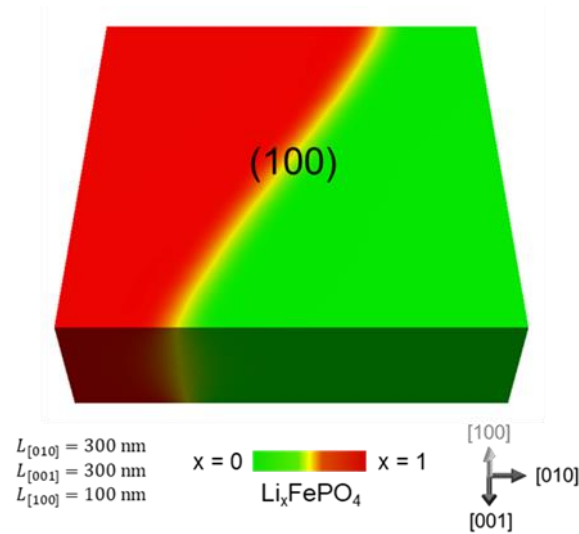
where R is the gas constant, T is the room temperature, F is the Faraday constant, and η is the electrochemical overpotential calculated in galvanostatic voltage graph shown in Supplementary Fig. 1(b).

- 4) To reduce the uncertainty arising from the time-averaged current density between two Li maps, we calculated the normalized current density $\tilde{j}_{0\text{Ch}}$ by fitting $j_{0\text{Ch}}$ with the following equation (5)^{7,17,18}

$$j_{0\text{Ch}}(x) = 3k_0(1-x)\sqrt{x(1-x)}. \quad (5)$$

k_0 is a fitting parameter, and represents the magnitude of the exchange current density. $\tilde{j}_{0\text{Ch}}$ is equivalent to $j_{0\text{Ch}}(x)/k_0$. Additionally, in Fig. 4(b) in the main text, the equation for the solid-line, which were used for a guide to the eye, is $3(1-x)\sqrt{x(1-x)}$.

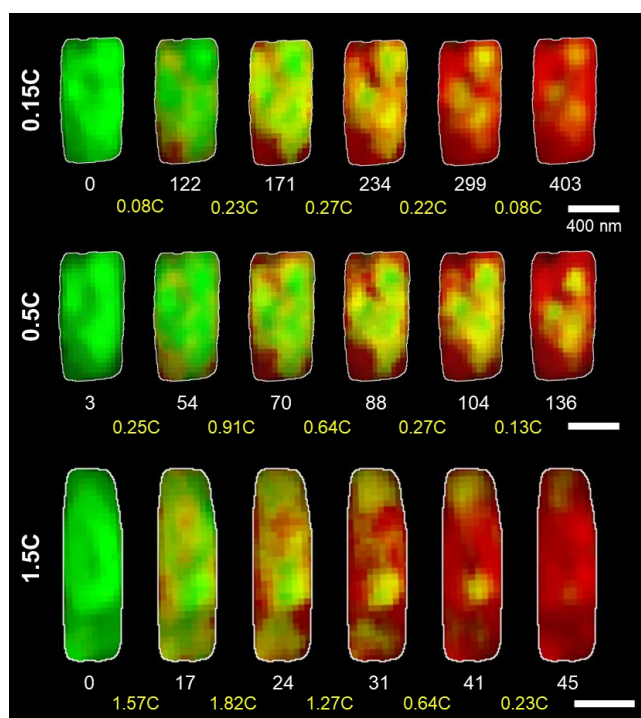
Supplementary section 11. Description for 3D phase field model and 3D relaxation simulation



Supplementary Fig. 11 3D phase field simulation for relaxation of [100]-oriented LFP

To understand the phase morphologies under insertion and relaxation, we performed 3D phase-field simulations on a single Li_xFePO_4 particle with dimensions of $300 \text{ nm} \times 300 \text{ nm} \times 100 \text{ nm}$. Our goal is to investigate the simulated phase morphologies during insertion in the [010]-direction and compare with our experimental observations. The eigenstrain in the crystallographic [010] direction is assumed to be linear with respect to Li composition, with a constant chemical expansion coefficient of 0.0346, consistent with previous computational studies.^{19–21} The gradient energy penalty is isotropic (equal in all directions). For relaxation, the diffusivity in [010] direction is taken to be $10^{-9} \text{ cm}^2/\text{s}$, consistent with first-principles calculations.²² The particle is subject to zero external force ($n \cdot \sigma = 0$) and the strain fields are considered to be coherent. The set of differential equations of our model was discretized using finite elements, and all unknowns were approximated with linear polynomial basis functions.²³ For the time integration of the resulting system of differential algebraic equations, we used 2nd order Gear method.

Supplementary section 12. Representative *operando* STXM results during lithiation at various C-rates



Supplementary Fig. 12 Representative particles captured via *operando* STXM during lithiation at various C-rates. Images at 0.15C were obtained from Fig. 3(a) in the main text for comparison. Scale bars, 400 nm.

References

1. Lim, J. *et al.* Origin and hysteresis of lithium compositional spatiodynamics within battery primary particles. *Science* **353**, 566–571 (2016).
2. Li, Z. *et al.* [100]-Oriented LiFePO₄ Nanoflakes toward High Rate Li-Ion Battery Cathode. *Nano Lett.* **16**, 795–799 (2016).
3. Coelho, A. A. TOPAS and TOPAS-Academic: An optimization program integrating computer algebra and crystallographic objects written in C++: *An. J. Appl. Crystallogr.* **51**, 210–218 (2018).
4. Chen, J. & Graetz, J. Study of antisite defects in hydrothermally prepared LiFePO₄ by in situ x-ray diffraction. *ACS Appl. Mater. Interfaces* **3**, 1380–1384 (2011).
5. Li, Y. *et al.* Dichotomy in the Lithiation Pathway of Ellipsoidal and Platelet LiFePO₄ Particles Revealed through Nanoscale Operando State-of-Charge Imaging. *Adv. Funct. Mater.* **25**, 3677–3687 (2015).
6. Ohmer, N. *et al.* Phase evolution in single-crystalline LiFePO₄ followed by in situ scanning X-ray microscopy of a micrometre-sized battery. *Nat. Commun.* **6**, 1–7 (2015).
7. Lim, J. *et al.* Origin and hysteresis of lithium compositional spatiodynamics within battery primary particles. *Science* **353**, 566–571 (2016).
8. Csernica, P. M. *et al.* Persistent and partially mobile oxygen vacancies in Li-rich layered oxides. *Nat. Energy* **6**, 642–652 (2021).
9. Mefford, J. T. *et al.* Correlative operando microscopy of oxygen evolution electrocatalysts. *Nature* **593**, (2021).
10. De Smit, E. *et al.* Nanoscale chemical imaging of a working catalyst by scanning transmission X-ray microscopy. *Nature* **456**, 222–225 (2008).
11. Yoo, M. *et al.* A tailored oxide interface creates dense Pt single-atom catalysts with high catalytic activity. *Energy Environ. Sci.* **13**, 1231–1239 (2020).
12. Park, J. *et al.* Fictitious phase separation in Li layered oxides driven by electroautocatalysis. *Nat. Mater.* **20**, 991–999 (2021).
13. Fraggedakis, D. *et al.* A scaling law to determine phase morphologies during ion intercalation. *Energy Environ. Sci.* 22–27 (2020).
14. Liu, H. *et al.* Capturing metastable structures during high-rate cycling of LiFePO

- 4 nanoparticle electrodes. *Science* **344**, (2014).
15. Zhang, X. *et al.* Direct view on the phase evolution in individual LiFePO₄ nanoparticles during Li-ion battery cycling. *Nat. Commun.* **6**, 1–7 (2015).
 16. Li, Y. *et al.* Fluid-enhanced surface diffusion controls intraparticle phase transformations. *Nat. Mater.* **17**, 915–922 (2018).
 17. Zhao, H. & Bazant, M. Z. Population dynamics of driven autocatalytic reactive mixtures. *Phys. Rev. E* **100**, 1–11 (2019).
 18. Bazant, M. Z. Thermodynamic stability of driven open systems and control of phase separation by electro-autocatalysis. *Faraday Discuss.* **199**, 423–463 (2017).
 19. Cogswell, D. A. & Bazant, M. Z. Coherency strain and the kinetics of phase separation in LiFePO₄ nanoparticles. *ACS Nano* **6**, 2215–2225 (2012).
 20. Bai, P., Cogswell, D. A. & Bazant, M. Z. Suppression of phase separation in LiFePO₄ nanoparticles during battery discharge. *Nano Lett.* **11**, 4890–4896 (2011).
 21. Tang, M., Belak, J. F. & Dorr, M. R. Anisotropic phase boundary morphology in nanoscale olivine electrode particles. *J. Phys. Chem. C* **115**, 4922–4926 (2011).
 22. Nadkarni, N. *et al.* Interplay of phase boundary anisotropy and electro-autocatalytic surface reactions on the lithium intercalation dynamics in LiXFePO₄ plateletlike nanoparticles. *Phys. Rev. Mater.* **2**, 1–13 (2018).
 23. Fraggedakis, D., Papaioannou, J., Dimakopoulos, Y. & Tsamopoulos, J. Discretization of three-dimensional free surface flows and moving boundary problems via elliptic grid methods based on variational principles. *J. Comput. Phys.* **344**, 127–150 (2017).